M. Manetti, M. Morandini, P. Mantegazza
Self-Tuning Shape Control of Massively Actuated Adaptive Mirrors
IEEE Transactions on Control Systems Technology, Vol. 22, N. 3, 2014, p. 838-852
doi:10.1109/TCST.2013.2267814

Self-tuning shape control of massively actuated adaptive mirrors

Mauro Manetti, Marco Morandini and Paolo Mantegazza

Abstract

This paper focuses on the design of the control system of massively actuated deformable mirrors for astronomical adaptive optics applications. The proposed solution is based on a high frequency completely decentralized feedback combined with a hybrid low frequency term, that is the sum of feedforward-feedback contributions. An appropriate in the field system identification procedure and an automatic gain optimization eventually lead to a complete self-tuning controller. The improvements of system performances are evaluated through high fidelity simulations.

Index Terms

Adaptive optics, Secondary deformable mirror, Feedforward control, Decentralized control, Self-tuning control

I. Introduction

Adaptive optics allows to compensate image distortions of astronomical observations introduced by atmospheric turbulence; this is achieved through the active control of the shape of a mirror. The system is usually structured in multilevel nested closed loops; as shown in Fig.1 the image residual wavefront aberrations are measured by the wavefront sensor, the optical controller elaborates the optimal shape command to compensate for image distortion and the adaptive mirror tracks the required shapes [1].

This paper focuses on the inner control loop required by secondary deformable mirrors (DMs) to track commanded shapes. The control technology is based on non-contacting voice-coil actuators, co-located to capacitive position sensors. A detailed description of the system

Mauro Manetti (e-mail: mauro.manetti@mail.polimi.it), Marco Morandini (e-mail: marco.morandini@polimi.it) and Paolo Mantegazza (e-mail: paolo.mantegazza@polimi.it) are with Politecnico di Milano, Dipartimento di Scienze e Tecnologie Aerospaziali, via La Masa 34, 20156 Milano, Italy.

Corresponding author: Marco Morandini (e-mail: marco.morandini@polimi.it)

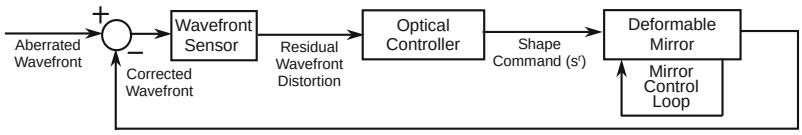

Figure 1. Adaptive optics control system.

model and of an enhanced controller can be found in [2], [3], [4]. The control law proposed in the above mentioned papers is based on already working solutions, such as the Multiple Mirror Telescope (MMT) [5] and the Large Binocular Telescope (LBT) [6].

The design of control systems for deformable shells sized in the order of meters and with thousands of control points represents a real challenge. Large shells are characterized by an high modal density; the well-known relation between signal attenuation and phase lag prevents the introduction of a sufficient attenuation on a significant portion of modal shapes beyond the control bandwidth. These facts, together with the low damping factors of high modes, are the critical issues for this kind of control problem. The strong coupling between the control points would suggest the adoption of completely centralized controllers, but the technological realization complexity and the time required to acquire, condition and process all the control signals prevent this choice. More appropriate approaches appear to be distributed control techniques [7], [8], [9], [10], [11], even if they would require a not negligible hardware update to be implemented. A distributed control feedback would certainly be an improvement with respect to a simpler completely decentralized solution. However, most of the positioning and tracking accuracy is granted, for the case at hand, by a feedforward term; for this reason the improvements brought by a distributed feedback solution may be considered limited if weighted with the required hardware update.

The aim of the present paper is to provide a complement to the controller introduced in [2], which is based on a completely decentralized high frequency feedback, combined with a low-frequency term which is the sum of pure feedforward (FF) contributions plus a hybrid feedforward-feedback term, here dubbed HFF. The complemented points are the stabilization of the HFF contribution of [2], the presentation of a self-tuning control procedure based both on the identification of static and dynamic FF matrices and on the optimization of few system parameters.

The outline of the paper is as follows. Section II briefly summarizes the detailed non-linear system model that is exploited to perform the simulations. Section III deals with the control strategy. The control structure of [2] is the sum of a feedback (Section III-B) and a

feedforward (Section III-C). The feedforward contribution of [2], however, is implemented with a recursive scheme (see [2] and Section III-D for details). As already shown in [4], the effect of this particular implementation can be reinterpreted as the sum of a feedforward and of a centralized integral feedback action; however, the actual implementation is that of a single, somewhat strange feedforward term. This kind of implementation is useful in order to reduce the actual computational cost of the controller and can be easily implemented on existing systems. As shown in Sec. III-G the resulting centralized integral has a significantly improved bandwidth with respect to a decentralized integral implementation; however, by not splitting the feedforward and integral feedback, does not easily allow to set the integral gain, paving the way for possible instabilities. Two different stabilization schemes for the HFF contribution are thus proposed in Section III-D. The feedforward control scheme matrices should be identified in the field, on the real hardware, that here is substituted by the detailed nonlinear simulation model of Section II. Section III-E proposes a possible identification procedure of the above mentioned matrices. The control system parameters can be tuned in site; the identification of the feedforward matrices is the first step of the tuning procedure. After that, there remains to tune six scalar parameters, i.e. three decentralized feedback gains, a scalar HFF stabilization coefficient and two additional feedforward scaling factors. Their optimal value can be searched automatically, as explained in Section III-F. The proposed control scheme proves to give substantial performance improvements even if decentralized feedback gains assuring stability robustness, as computed in Section III-G, are used instead of the optimized ones. Section III-G also points out the relevance of low-pass filtering the measurements and control forces, as well as the effect on system stability of the spatial filter action introduced by the capacitive position sensors. The effectiveness of the proposed solution is verified in Section IV through high fidelity simulations of the adaptive secondary mirror of the Giant Magellan Telescope (GMT) [12]. The GMT secondary optics is based on seven Zerodur mirrors, with 1 m diameter and 672 actuators each, for a total of 4,704 control points. The seven secondary mirrors are statically and dynamically decoupled, so all the analysis presented in this work refer to the single on-axis DM, whose behavior is considered to be representative of all the other ones.

II. SYSTEM MODEL

As shown in Fig. 2, the secondary adaptive mirrors under investigation are characterized by a thin ($1-2$ mm) deformable shell; their shape is controlled through the action of electro-

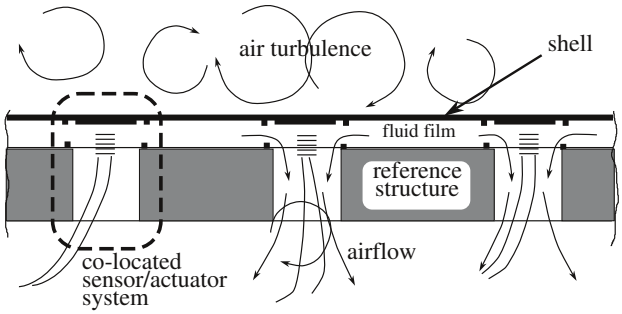

Figure 2. Section sketch of the mirror shell and reference structure [2].

magnetic voice-coil motors and measured by capacitive position sensors. The system behavior and performances are highly affected by the fluid dynamic forces exerted by the air squeeze film interposed within the thin gap ($30 - 120$ μm) that separates the deformable shell and the stiff reference structure. Air turbulence, acting on the reflecting mirror surface, is one of the main source of disturbances.

The resulting multiphysics problem has been handled through the development of appropriate models and ad hoc simulation tools. An accurate description of all the modeling choices, together with further details about the simulation code implementation and its ability to correlate with experimental data have already been presented in previous works [2], [13], [14], [3]. The aim of such detailed modeling is the development of an accurate simulator, not a system description suitable for the control system design. Despite this fact the development of an accurate model can be even exploited to suggest and verify simplified descriptions more adequate to the control design.

Starting from a Finite Element (FE) scheme, a reduced model is obtained through a normal vibration modes condensation, so to guarantee a correct structural dynamics description within the frequency band of interest. The $(n_g \times 1)$ FE nodal displacement vector $\boldsymbol{x}$ can be approximated as $\boldsymbol{x} \approx \boldsymbol{X}_g \boldsymbol{q}$, where $\boldsymbol{q}$ is the chosen set of n_m generalized modal coordinates and $\boldsymbol{X}_g$ is the $(n_g \times n_m)$ modal shape matrix. Choosing a unit modal mass normalization and a diagonal modal damping, the uncoupled equation of motion of the i^{th} mode is

$$\ddot{q}_i + 2\xi_i \omega_i \dot{q}_i + \omega_i^2 q_i = f_{m_i}^c + f_{m_i}^t + f_{m_i}^f, \tag{1}$$

where q_i is the modal degree of freedom and ω_i, ξ_i are its natural frequency and damping coefficient. The control, air turbulence disturbance and fluid film n_m generalized $(n_m \times 1)$ modal force vectors are given by $\boldsymbol{f}_m^c = \boldsymbol{X}^T \mathrm{sat}(\boldsymbol{f}_a^c)$, $\boldsymbol{f}_m^t = \boldsymbol{X}^T \boldsymbol{f}_a^t$ and $\boldsymbol{f}_m^f = \boldsymbol{X}_f^T \boldsymbol{f}^f$; here the element (i, j) of the $(n_a \times n_m)$ condensed mode shape matrix $\boldsymbol{X} = \boldsymbol{B}_x^T \boldsymbol{X}_g$ represents

the displacement of the i^{th} actuator associated to the j^{th} normal mode and $\mathrm{sat}()$ accounts for possible actuators saturation; in the same way the $(n_f \times n_m)$ matrix $\boldsymbol{X}_f = \boldsymbol{B}_f^T \boldsymbol{X}_g$ describes the modal shapes corresponding to the fluid dynamic nodes, with $\boldsymbol{B}_x$ and $\boldsymbol{B}_f$ the $(n_g \times n_a)$ and $(n_g \times n_f)$ control forces and fluid dynamic influence matrices.

A description of the adopted simplified turbulence disturbance modeling can be found in [4]; it is here considered fully correlated over the mirror and the disturbance time history is obtained from a first order rational approximation of its Von Karman power spectrum.

The voice-coil actuators forces are considered to be ideally applied pointwise and acting normally to the deformable shell. Possible couples introduced by the actuators are considered negligible; furthermore, the misalignment of their forces with respect to the shell normal direction do not imply significant shell deformations. The actuators dynamics are described through uncoupled, up to second order, models

$$\dot{\boldsymbol{x}}_f = -\left[\diagdown \boldsymbol{A}_f \diagdown\right] \boldsymbol{x}_f + \left[\diagdown \boldsymbol{B}_f \diagdown\right] \boldsymbol{f}^c, \quad \boldsymbol{f}_a^c = \left[\diagdown \boldsymbol{C}_{\boldsymbol{f}} \diagdown\right] \boldsymbol{x}_f, \tag{2}$$

where $\boldsymbol{f}^c$ represents the $(n_a \times 1)$ required control forces vector and the matrices $\left[\diagdown \boldsymbol{A}_f \diagdown\right]$ (n_a 2×2 blocks), $\left[\diagdown \boldsymbol{B}_{\boldsymbol{f}} \diagdown\right]$ (n_a 2×1 blocks) and $\left[\diagdown \boldsymbol{C}_{\boldsymbol{f}} \diagdown\right]$ (n_a 1×2 blocks) are block diagonal; diagonal matrices will be characterized by a bracketed notation throughout all the paper.

As a first approximation the measures obtained through the capacitive position sensors can also be considered ideally pointwise and co-located with the actuation forces; the normal shell displacements at each actuation point, $\boldsymbol{d}$ $(n_m \times 1)$, is retrieved from the simulation as $\boldsymbol{d} = \boldsymbol{X}\boldsymbol{q}$. Fig. 3 shows the ideal co-located position of all the GMT mirror controlled points with black dots and the gray circular coronas representing the capacitors plates, where the variable capacitance is measured. It is clear that the capacitor plates dimension is by no means negligible and that the non co-location may be significant in presence of sufficiently complex/wavy spatial deformations. As shown in [15] the non co-location of the measures can be modeled through the computation of the motion dependent variable capacitance of the sensors circular electrodes. The present work highlights the importance to model such a non co-location, not only in order to correctly estimate the required system control forces, as shown in [13], [14], but also to obtain a realistic evaluation of the system stability. In fact, the intrinsic distributed nature of the position measures acts as a band-stop spatial filter with respect to a non negligible portion of the structural modal shapes, so limiting possible instabilities linked to spillover phenomena (see Subsec. III-G).

The capacitance C_{mes} measured by each sensor is a non linear function of the local mirror

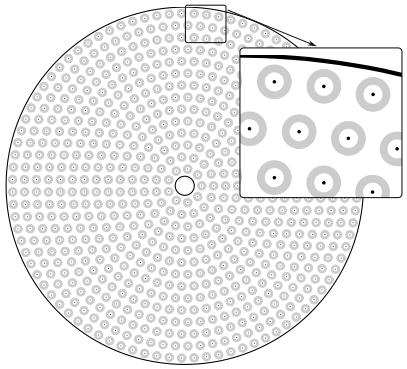

Figure 3. Sensor capacitor plates (gray circular coronas) and ideal co-located actuation points (black dots).

motion, $C_{mes} = \int_{\Sigma} \frac{\varepsilon}{x_{nc}} d\Sigma$, where ε is the absolute air dielectric constant, Σ is the surface of the capacitors circular coronae and x_{nc} is the pointwise distance of the capacitors plates. The sensor dynamics are introduced with an up to second order scheme, through the use of the non co-located measured capacitance

$$\dot{\boldsymbol{x}}_p = -\left[\diagdown \boldsymbol{A}_p \diagdown\right] \boldsymbol{x}_p + \left[\diagdown \boldsymbol{B}_p \diagdown\right] \boldsymbol{V}_{in}, \quad \boldsymbol{V}_{out} = \left[\diagdown \boldsymbol{C}_p \diagdown\right] \boldsymbol{x}_p, \tag{3}$$

where $\boldsymbol{V}_{in} = \boldsymbol{V}_{in}(\boldsymbol{C}_{mes})$ is the $(n_a \times 1)$ vector of the capacitance voltages, $\boldsymbol{V}_{out}$ is the $(n_a \times 1)$ vector of sensor voltage output and the block diagonal matrices are analogous to those of Eq. 2. The $(n_a \times 1)$ vector of measured positions, $\boldsymbol{p}$, is then related to $\boldsymbol{V}_{out}$ through an appropriate function, $\boldsymbol{p} = \boldsymbol{p}\,(\boldsymbol{V}_{out})$, so $\boldsymbol{p}$ represents the shell displacements on the actuation points, $\boldsymbol{d}$, obtained as output from capacitive sensors. It should be remarked that the functions $\boldsymbol{C}_{mes}$ and $\boldsymbol{p}$ are generally non linear, so even if the sensors dynamics appear as linear their overall functionality is not.

The force and position signals description is completed by introducing an appropriate representation of A/D/A conversions and computations errors and delays related to the digital controller, along with sensors and actuators noises.

The fluid film between the mirror and the reference plane has a thickness h of $30-120$ μm and it is usually called squeeze film. The squeeze film analysis is carried out through an ad hoc two dimensional formulation, based on Navier-Stokes equations. The discretization of the fluid dynamic equations has been based on a Finite Volume technique.

More details about the fluid dynamic model development, its Finite Volume implementation and the fluid-structure interface can be found in [3], [4]. The fluid dynamics system should not be overlooked. It proves to be crucial in providing a good correlation between numerical and experimental data, as shown in [14], [15], and heavily affects the shell dynamic response

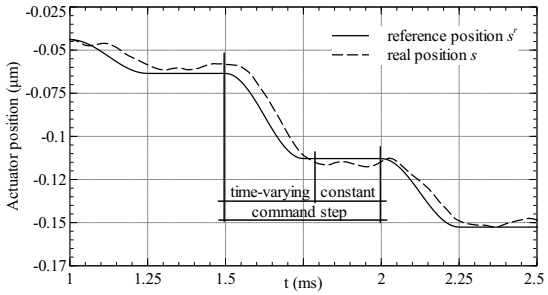

Figure 4. Sketch of typical time varying and constant commands, with the corresponding dynamic and steady mirror response, over command steps [2].

and its stability.

III. CONTROL STRATEGY

The DM control system is a refinement and completion of the solution already presented in [2]. The objective of the DM high-frequency controller (70-100 kHz) is to adjust the shape of the reflecting surface following a reference command. The reference command is generated by the optical control system and is sent to the DM controller as a relatively low-frequency ($250 - 2000$ Hz) step signal assigning the position that each actuator should reach. The mirror shape controller has to allow an as precise and fast as possible achievement of the commanded positions.

To limit the excitation of high-frequency modes and to help a smoother transition the $(n_a \times 1)$ reference step commands are shaped in time through jerk-free functions, $f_{sh}(t)$. In this way each command step is divided in two parts (see Fig. 4): the first one is time varying, the second constant. It is then possible to write the $k+1$ step command vector as

$$\boldsymbol{d}^r(t) = \boldsymbol{d}^r_{(k)} + (\boldsymbol{d}^r_{(k+1)} - \boldsymbol{d}^r_{(k)}) f_{sh}(t). \tag{4}$$

The use of pre-computed shaping functions has been preferred with respect to a more standard low-pass filter because it allows to avoid a causal step by step computation of the command signal: it suffices to simply store in advance on the system the unique geometric profile $f_{sh}(t)$ and to scale it by the command step amplitude.

The proposed solution is based on a two degrees of freedom controller. The theoretical advantage of a two degrees of freedom structure is the possibility of adjusting two different closed loop transfer functions independently. This approach is possible because the controller can separately treat the command signal $\boldsymbol{s}^r$ and the sensor measurements $\boldsymbol{p}$. Usually a single degree of freedom solution requires a trade-off between tracking performances and

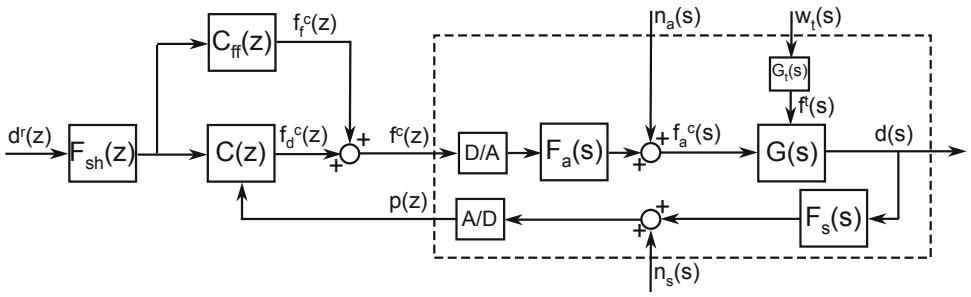

Figure 5. Block diagram of the proposed two degrees of freedom controller. $\boldsymbol{C}_{ff}(z)$ is the feedforward control block matrix, $\boldsymbol{C}(z)$ is the feedback controller block, $\boldsymbol{F}_a(s)$ is the actuators transfer matrix, $\boldsymbol{G}(s)$ is the fluid-elastic system transfer matrix, $\boldsymbol{G}_t(s)$ is the turbulence disturbance transfer matrix and $\boldsymbol{F}_s(s)$ is the sensors transfer matrix. The actuators and sensors noises are respectively $\boldsymbol{n}_a(s)$ and $\boldsymbol{n}_s(s)$, while $\boldsymbol{f}^t(s)$ represents the turbulence disturbance forces, obtained from the white disturbance $\boldsymbol{w}_t(s)$ shaped through the turbulence transfer matrix $\boldsymbol{G}_t(s)$. All the transfer matrices of the diagram blocks have dimension $(n_a \times n_a)$, while the input and output vectors have dimension $(n_a \times 1)$.

disturbance rejection; on the contrary, a two degrees of freedom controller allows to better satisfy both of the differing requirements [16, chap. 2.6.5] (see Sec. III-F). Among the possible implementations of a two degrees of freedom controller [17], we adopt a specialized and improved version based on a proportional-derivative (PD) feedback with system dynamics compensation through feedforward [18], [19] (see Fig. 5).

A. Proposed control law

It is clear that, for a perfectly known plant, without disturbances, the feedforward alone would allow to obtain the ideal input-output relation $\boldsymbol{d} = \boldsymbol{d}^r$, the so called "perfect control". The feedforward simply compensates the system own dynamics through an inverse-based controller. Of course this ideal result cannot be attained in practice, not only for the unavoidable presence of noises, disturbances, quantization errors and delays but also because one cannot realize an inverse system dynamics respecting the controller causality in presence of pure time delays and, possibly, right half plane zeros. Moreover without suitable feedback terms the plant dynamics compensation through a feedforward term does not yield sufficient performance robustness. An alternative approach is to change the FF in a feedback contribution, possibly adding an integral term to assure more performance robustness, such as for the so called torque [20] and internal model controls [21]. Both the feedback and the feedforward based techniques aim at an approximate system dynamics compensation and decoupling. This decoupling is a highly desirable feature since it allows to introduce a further feedback controller, based on SISO control loops, to determine the final

controlled system behavior. Unfortunately, in practice the realization of an approximated, but effective, inverse-based control for a wide frequency domain is not feasible. For this reason an acceptable decoupling and a compensation of the system dynamics is often sought at a particular frequency or within a convenient limited frequency range. Moreover, the feedback decoupling is very sensitive to modeling errors and can limit system stability, so that an inverse-based controller is usually not the best choice to reject disturbances [16]. Beyond these general issues one should consider that all the previous feedback based techniques require a centralized controller architecture but, as already mentioned in the introduction, a complete centralization is not practical for massively actuated large DMs.

The proposed solution is a centralized feedforward term, computed at a relatively low-frequency and then appropriately modified to include an integral feedback contribution as well (see Sec. III-D). This allows to approximately decouple the MIMO system while partially compensating its dynamics. Once an approximated decoupling has been obtained, a high-frequency, completely decentralized, feedback action provides an adequate system stability, while further improving the tracking performances. The system control force is thus the sum of a feedback and feedforward contribution, $\boldsymbol{f}_d^c$ and $\boldsymbol{f}_f^c$, i.e.$\boldsymbol{f}^c = \boldsymbol{f}_d^c + \boldsymbol{f}_f^c$.

B. Feedback contribution

The high-frequency feedback contribution has mainly to provide electronic damping to the modal shapes excited during the mirror deformation, while helping signal tracking; an help to system positioning and disturbance rejection is also introduced, even if its effectiveness on these two issues is limited and requires the introduction of a different term, i.e. the HFF contribution. The decentralized high-frequency feedback can be obtained by resorting to a PDD2 scheme

$$\boldsymbol{f}_{d(j)}^c = [\diagdown \boldsymbol{G}_{p} \diagdown] \left(\boldsymbol{d}_{(j)}^r - \boldsymbol{p}_{(j)}\right) + [\diagdown \boldsymbol{G}_{v} \diagdown] \left(\dot{\boldsymbol{d}}_{(j)}^r - \dot{\boldsymbol{p}}_{(j)}\right) + [\diagdown \boldsymbol{G}_{a} \diagdown] \left(\ddot{\boldsymbol{d}}_{(j)}^r - \ddot{\boldsymbol{p}}_{(j)}\right), \qquad (5)$$

where the index (j) varies over the high-frequency control steps and the $(n_a \times n_a)$ matrices $[\diagdown \boldsymbol{G}_{p} \diagdown]$, $[\diagdown \boldsymbol{G}_{v} \diagdown]$ and $[\diagdown \boldsymbol{G}_{a} \diagdown]$ are diagonal, so that n_a SISO control loops, coupled through the system dynamics, are introduced. The pseudo-derivative filters required to compute the velocity $\dot{\boldsymbol{p}}_{(j)}$ and acceleration $\ddot{\boldsymbol{p}}_{(j)}$ of the actuated points can be obtained by performing a design directly in the discrete time domain. The filters design usually looks for a tradeoff between noise attenuation and phase lag.

C. Feedforward contribution

The structure of the proposed feedforward term can be built by inverting an approximated system model transfer matrix $\boldsymbol{G}_n(s)$, with dimension $(n_a \times n_a)$. The structural dynamics can be approximated by $\boldsymbol{M}_s^*\ddot{\boldsymbol{d}} + \boldsymbol{C}_s^*\dot{\boldsymbol{d}} + \boldsymbol{K}^*\boldsymbol{d} + \boldsymbol{f}_c^{f*}(\boldsymbol{d}) = \boldsymbol{f}_a^c$, where $\boldsymbol{M}_s^*$, $\boldsymbol{C}_s^*$ and $\boldsymbol{K}^*$ are respectively the $(n_a \times n_a)$ structural mass, damping and stiffness matrices condensed at the actuation points, while $\boldsymbol{f}_c^{f*}(\boldsymbol{d})$ represents the $(n_a \times 1)$ vector of the squeeze film fluid dynamic forces, condensed at the actuation points as well. Let us assume also a quasi-steady description of the squeeze film forces, so that they can be approximated by $\boldsymbol{f}_c^{f*}(\boldsymbol{d}) = \boldsymbol{M}_f^*\ddot{\boldsymbol{d}} + \boldsymbol{C}_f^*\dot{\boldsymbol{d}}$, where $\boldsymbol{M}_f^*$ and $\boldsymbol{C}_f^*$ are suitable $(n_a \times n_a)$ fluid dynamic condensed mass and damping matrices. The nominal approximated plant transfer function becomes $\boldsymbol{G}_n(s) = (s^2\boldsymbol{M}^* + s\,\boldsymbol{C}^* + \boldsymbol{K}^*)^{-1}$, with $\boldsymbol{M}^* = (\boldsymbol{M}_s^* + \boldsymbol{M}_f^*)$ and $\boldsymbol{C}^* = (\boldsymbol{C}_s^* + \boldsymbol{C}_f^*)$ being the $(n_a \times n_a)$ mass and damping matrices of the simplified control model; the corresponding inverse-based FF transfer function $\boldsymbol{C}_{ff}(s)$ could be chosen as

$$\boldsymbol{C}_{ff}(s) = \boldsymbol{G}_n^{-1}(s) = s^2\boldsymbol{M}^* + s\,\boldsymbol{C}^* + \boldsymbol{K}^*. \tag{6}$$

The corresponding discrete form will be introduced in a natural way later on (see Eq. 8). Eq. 6 allows to obtain the FF contribution in the time domain as

$$\boldsymbol{f}_f^c(t) = \mathcal{L}^{-1}\left(\boldsymbol{C}_{ff}\boldsymbol{F}_{sh}\boldsymbol{d}^r\right) = \boldsymbol{M}^*\ddot{\boldsymbol{d}}^r(t) + \boldsymbol{C}^*\dot{\boldsymbol{d}}^r(t) + \boldsymbol{K}^*\boldsymbol{d}^r(t). \tag{7}$$

The discrete realization of the FF action can be simply obtained by substituting Eq. 4 into Eq. 7 evaluated at the discrete time $t_{(j)}$

$$\begin{aligned}\boldsymbol{f}_{f(j)}^c =& \boldsymbol{M}^*\left(\boldsymbol{d}_{(k+1)}^r - \boldsymbol{d}_{(k)}^r\right)\ddot{f}_{sh}(t_{(j)}) + \boldsymbol{C}^*\left(\boldsymbol{d}_{(k+1)}^r - \boldsymbol{d}_{(k)}^r\right)\dot{f}_{sh}(t_{(j)}) + \\ & \boldsymbol{K}^*\boldsymbol{d}_{(k)}^r + \boldsymbol{K}^*\left(\boldsymbol{d}_{(k+1)}^r - \boldsymbol{d}_{(k)}^r\right) f_{sh}(t_{(j)}),\end{aligned} \tag{8}$$

where the index (j) varies over the high-frequency control steps, while the index (k) refers to the low-frequency command rate. The unknown approximated plant matrices $\boldsymbol{M}^*$, $\boldsymbol{C}^*$ and $\boldsymbol{K}^*$, on which the feedforward is based, can be obtained through a very efficient in the field identification procedure described in Sec. III-E.

The FF contribution $\boldsymbol{f}_f^c$ can be interpreted as the sum of a dynamic and a static term ($\boldsymbol{f}_{fd}^c$ and $\boldsymbol{f}_{fs}^c$ respectively), $\boldsymbol{f}_f^c = \boldsymbol{f}_{fd}^c + \boldsymbol{f}_{fs}^c$, where

$$\boldsymbol{f}_{fd(j)}^c = \boldsymbol{M}^*\left(\boldsymbol{d}_{(k+1)}^r - \boldsymbol{d}_{(k)}^r\right)\ddot{f}_{sh}(t_{(j)}) + \boldsymbol{C}^*\left(\boldsymbol{d}_{(k+1)}^r - \boldsymbol{d}_{(k)}^r\right)\dot{f}_{sh}(t_{(j)}), \tag{9}$$

$$\boldsymbol{f}_{fs(j)}^c = \boldsymbol{K}^*\boldsymbol{d}_{(k)}^r + \boldsymbol{K}^*\left(\boldsymbol{d}_{(k+1)}^r - \boldsymbol{d}_{(k)}^r\right) f_{sh}(t_{(j)}). \tag{10}$$

The identified matrix $\boldsymbol{K}^*$ is a close relative of the true mirror stiffness condensed at the actuation points; in practice it differs from it mainly because of the sensors non co-location [15]. The static FF contribution thus gives the static forces required to deform the mirror. The shell stiffness is the main coupling element of the system, and the static FF provides a fundamental decoupling action. This was a key point from the very first applications [22] because the completely decentralized feedback contribution alone is not able to guarantee the required system static deformation because of the intrinsic coupled nature of the elastic problem, together with a severe limitation to the gains imposed by stability constraint. The dynamic FF is based on the identified matrices $\boldsymbol{M}^*$ and $\boldsymbol{C}^*$, which have a strong diagonal dominance, so suggesting that this FF contribution is not fundamental to decouple the open loop system transfer matrix. Nevertheless, its contribution substantially improves the system tracking performances during the time-varying part of the step by partly compensating the open-loop system dynamics, so that the closed-loop dynamics can be determined mainly by the feedback controller.

It is important to note that the FF contributions require a completely centralized computation; however Eq. 8 makes it clear that the matrix-vector products needed to compute the feedforward terms are carried out just once for each command step k. This means that the centralized computation is required at the low command frequency, while the high-frequency time shaping through the scalar function $f_{sh}(t_{(j)})$ is a completely decentralized operation.

D. From feedforward to feedback: the HFF contribution

The $(n_a \times 1)$ steady state position error vector $\boldsymbol{e}_0 = \boldsymbol{d}^r - \boldsymbol{p}$ can be caused by a step change of the reference command $\boldsymbol{d}^r$, by a constant step disturbance $\boldsymbol{w}_{t_0}$, or by the actuator noise $\boldsymbol{n}_{a_0}$, and can be expressed as

$$\boldsymbol{e}_0 = \left(\boldsymbol{I} + \boldsymbol{F}_{s_0}\boldsymbol{K}^{*^{-1}}\boldsymbol{F}_{a_0}\left[\diagdown \boldsymbol{G}_p \diagdown\right]\right)^{-1}\left[\left(\boldsymbol{I} - \boldsymbol{F}_{s_0}\boldsymbol{K}^{*^{-1}}\boldsymbol{F}_{a_0}\boldsymbol{C}_{ff_0}\right)\boldsymbol{d}^r - \boldsymbol{F}_{s_0}\boldsymbol{K}^{*^{-1}}\left(\boldsymbol{n}_{a_0} + \boldsymbol{G}_{\boldsymbol{t_0}}\boldsymbol{w}_{t_0}\right)\right]. \tag{11}$$

In Eq. 11 the subscript $[\,]_0$ refers to transfer matrices evaluated at $s = 0$; the feedback control law has been explicitly introduced at $s = 0$, i.e. $\boldsymbol{C}(s) = \left[\diagdown \boldsymbol{G}_p \diagdown\right]$. The transfer matrix $\boldsymbol{C}_{ff_0}$ represents the static FF contribution, that, under the hypothesis of a perfect static FF matrix identification, can drive the term $\left(\boldsymbol{I} - \boldsymbol{F}_{s_0}\boldsymbol{K}^{*^{-1}}\boldsymbol{F}_{a_0}\boldsymbol{C}_{ff_0}\right)$ to zero . In practice an exact cancellation is unobtainable, so there is always a residual steady state error due to a step command, combined with the contributions from steady external disturbances and, possibly,

steady components of the actuators noise. Eq. 11 is then rewritten as

$$\boldsymbol{e}_0 = \left(\boldsymbol{I} + \boldsymbol{F}_{s_0}\boldsymbol{K}^{*^{-1}}\boldsymbol{F}_{a_0}\left[\diagdown \boldsymbol{G}_{p} \diagdown\right]\right)^{-1}\boldsymbol{v}_0, \tag{12}$$

where the $(n_a \times 1)$ vector $\boldsymbol{v}_0$ includes the sum of the three possible steady state error sources. Eq. 12 shows that the steady state error is scaled by the $(n_a \times n_a)$ sensitivity matrix $\boldsymbol{S}$, evaluated at $s = 0$

$$\boldsymbol{S}_0 = \boldsymbol{S}(s)|_{s=0} = \left(\boldsymbol{I} + \boldsymbol{F}_{s_0}\boldsymbol{K}^{*^{-1}}\boldsymbol{F}_{a_0}\left[\diagdown \boldsymbol{G}_{p} \diagdown\right]\right)^{-1}. \tag{13}$$

The 2-norm of the steady state error vector can be bounded by exploiting the sensitivity matrix singular values $\sigma()$ [16]

$$\underline{\sigma}\left(\boldsymbol{S}_0\right) \leq \frac{\|e_0\|_2}{\|v_0\|_2} \leq \bar{\sigma}\left(\boldsymbol{S}_0\right), \tag{14}$$

where $\underline{\sigma}()$ and $\bar{\sigma}()$ are the minimum and maximum singular values, respectively. In the simplified hypothesis of equal proportional gains for all the actuation points, i.e. $\left[\diagdown \boldsymbol{G}_{p} \diagdown\right] = G_p\boldsymbol{I}$, it is possible to provide a simple relation between the proportional gain value, G_p, the system stiffness matrix singular values and the steady state error bounds

$$\frac{\underline{\sigma}\left(\boldsymbol{K}^*\right)}{\underline{\sigma}\left(\boldsymbol{K}^*\right) + G_p} \leq \frac{\|e_0\|_2}{\|v_0\|_2} \leq \frac{\bar{\sigma}\left(\boldsymbol{K}^*\right)}{\bar{\sigma}\left(\boldsymbol{K}^*\right) + G_p}. \tag{15}$$

Focusing on the upper error bound, it is evident that an important reduction of the steady state error requires a proportional gain that is at least comparable to the highest stiffness matrix singular value; the latter coincides with the maximum stiffness matrix eigenvalue because $\boldsymbol{K}^*$ is a symmetric positive definite matrix. However, the experience on existing mirrors confirms that the proportional gain can at most reach roughly 5% of the maximum stiffness singular value without endangering the system stability. For this reason the steady position accuracy is highly dependent upon the static FF contribution accuracy, i.e. from the accuracy of the identified $\boldsymbol{K}^*$ matrix.

A robust zero steady state error, be it due to a step change of the reference position, to the introduction of a step disturbance or to a noise, can be achieved with an integral action inside the control loop, along with an ideally exact position measure. Of course the position measurements are always affected by errors and noises, but it can be reasonably assumed that the sensor has been designed in order to guarantee a satisfactory measurement precision. The outer optical feedback loop always contains an integral term; an integrator within the DM controller is however mandatory because the system is required to satisfy tracking and positioning specifications even when the optical loop is deactivated. An integral feedback

contribution could be easily introduced by adopting a decentralized PIDD2 feedback instead of the proposed PDD2. However a decentralized integral action would cause a degradation of the step response transient performances (e.g. Chapter 8 [23]). Moreover it would not be effective in presence of fast command rates, as the integral gains are severely limited by stability constraints. A more interesting solution, proposed in [2], can be obtained by modifying the static FF term defined in Eq. 10 as

$$\boldsymbol{f}^c_{fs(j)} = \overline{\boldsymbol{f}}^c_{(k)} + \boldsymbol{K}^* \left(\boldsymbol{d}^r_{(k+1)} - \overline{\boldsymbol{p}}_{(k)} \right) f_{sh}(t_{(j)}), \tag{16}$$

where the overline stands for the time average computed over the final part of the previous command step k. It is thus assumed that every actuator can achieve a stable average position by applying a steady average control force. The possibility of computing meaningful values for the averages $\overline{\boldsymbol{p}}$ and $\overline{\boldsymbol{f}}^c$ relies on a well defined transient, followed by a final steady part of each command step. Actually Eq. (16) allows to achieve a high gain feedback from a feedforward term at a relatively low command frequency. As shown in [4] the final steady value for each command step of the feedforward $\boldsymbol{f}^c_{fs}$ can be rewritten as

$$\boldsymbol{f}^c_{fs(k+1)} = \boldsymbol{K}^* \boldsymbol{d}^r_{(k+1)} - (\boldsymbol{K}^* + [\diagdown \boldsymbol{G}_{p} \diagdown]) \sum_{i=1}^{k} \left(\overline{\boldsymbol{p}}^{err}_{(i)} \right), \tag{17}$$

where $\overline{\boldsymbol{p}}^{err}_{(i)}$ is the error of the measured steady average position with respect to that requested at the i^{th} command step. The first right hand term of Eq. (17) represents the usual static feedforward contribution presented in Eq. 10, while the second term appears clearly as an integral coupled feedback action, applied at the slow command frequency, but with a centralized gain structure represented by the sum of the identified static FF matrix, $\boldsymbol{K}^*$, and the proportional gain matrix, $[\diagdown \boldsymbol{G}_{p} \diagdown]$. However, Eq. 16 should be preferred to Eq. 17 because represents a really efficient implementation, as it leads to a centralized FF and feedback contribution through a single matrix-vector product and with a little modification of the actual control system; the resulting computational time saving could be important for the feasibility of future extremely large telescopes.

Such a recursive feedforward allows to achieve an acceptable static response even if the estimated matrix $\boldsymbol{K}^*$ differs significantly from the actual one, the static error $\overline{\boldsymbol{p}}_{err}$ being quickly damped out thanks to the integral feedback contribution [2]. At the same time, it improves the system performance robustness with respect to slowly varying external noises and disturbances, such as the turbulence acting on the secondary adaptive mirror [4].

The unavoidable drawback of this scheme is that, by changing a mere feedforward into a feedforward-feedback contribution, it is possible to induce a system instability. Moreover, even if the system remains stable, the HFF performances can be partly compromised when the hypothesis of obtaining steady responses at the end of each command step is not verified. This is the case when the system is driven at high command rates or in presence of time varying external disturbances which impede to reach a well settled condition. For this reason we propose the following stabilization technique

$$\boldsymbol{f}^c_{f_s(j)} = [\diagdown \boldsymbol{\alpha} \diagup]\, \overline{\boldsymbol{f}}^c_{(k)} + (\boldsymbol{I} - [\diagdown \boldsymbol{\alpha} \diagup])\, \boldsymbol{f}^c_{f_s(k)} + \boldsymbol{K}^* \left(\boldsymbol{d}^r_{(k+1)} - \left([\diagdown \boldsymbol{\alpha} \diagup]\, \overline{\boldsymbol{p}}_{(k)} + (\boldsymbol{I} - [\diagdown \boldsymbol{\alpha} \diagup])\, \boldsymbol{d}^r_{(k)} \right) \right) f_{sh}(t_{(j)}), \tag{18}$$

where the parameter α_i, i.e. the i^{th} diagonal element of the matrix $[\diagdown \boldsymbol{\alpha} \diagup]$, can switch the static FF contribution of the i^{th} actuator from the implementation without any feedback contribution, $\alpha_i = 0$, to the full HFF solution, $\alpha_i = 1$.

The stabilizing scheme of Eq. 18 can be exploited through two different approaches. The first one works with a discrete set of values for α_i, that can either be equal to one or to zero. The value assigned to α_i depends on two conditions that must be checked for the i^{th} actuator. The first condition is related to the effective possibility of improving the system positioning on the base of the available accuracy on the related measurements

$$\overline{\boldsymbol{p}}_{(k_i)} - \boldsymbol{d}^r_{(k_i)} > \delta p_{quant}, \tag{19}$$

with δp_{quant} being the capacitive sensor resolution; this condition has been defined because it is not useful to try the correction of a steady position when the error is within the sensor resolution threshold. The second condition is directly related to the effective steadiness of the response during the constant part of the command step, and reads

$$\sigma\left(p_i\right) \leq \sigma_s + \delta\sigma, \tag{20}$$

with $\sigma\left(p_i\right)$ being the standard deviation of the position measurements over the steady part of the step, i.e. where the position and force averages are performed, σ_s the measurement noise standard deviation and $\delta\sigma$ a tunable parameter, that can be set as a fraction of the noise standard deviation σ_s. This condition guarantees that the motion at the i^{th} actuator is almost steady and it is the key point in avoiding the birth of instabilities or the degradation of the HFF performances due to non steady responses.

Both Eqs. (19, 20) should be verified in order to apply the HFF control, i.e. to set $\alpha_i = 1$. This approach allows to activate or deactivate the recursive feedforward just at a single

actuation point for a particular step command. Note that, whenever the recursive feedforward is deactivated over one or more command steps, all the previous integral contributions added to the actuation point are not lost but automatically kept in memory, thanks to the recursive implementation of the static FF term. The main drawback of this approach is that the feedback contribution could be completely deactivated when the HFF scheme makes the system unstable or in presence of a strong disturbance together with a too strict standard deviation limit $\sigma_s + \delta\sigma$. In this way the stability can be guaranteed but the integral action may be completely lost or carried out just at few actuation points.

A second approach is based on the idea that the parameter α can freely assume all the values in the range $[0-1]$. Following exactly the same steps leading to Eq. (17), one obtains

$$\boldsymbol{f}^c_{f_s(k+1)} = \boldsymbol{K}^* \boldsymbol{d}^r_{(k+1)} - \left[\diagdown \boldsymbol{\alpha} \diagdown\right] \left(\boldsymbol{K}^* + \left[\diagdown \boldsymbol{G}_{p} \diagdown\right]\right) \sum_{i=1}^{k} \left(\overline{\boldsymbol{p}}^{err}_{(i)}\right). \tag{21}$$

Eq. 21 simply means that the $\left[\diagdown \boldsymbol{\alpha} \diagdown\right]$ matrix acts as a scaling parameter with respect to the integral HFF gain. The system stability can then be guaranteed for all of the working conditions by setting a sufficiently low scaling matrix $\left[\diagdown \boldsymbol{\alpha} \diagdown\right]$. This solution allows to obtain a continuous action and assures the stability and a continuously updated integral contribution at the same time, even in presence of unsettled command step responses.

In practice Eq. 18 introduces the possibility to tune the gain of the feedback contribution within the HFF term and at the same time assures an efficient computation because both the feedback and FF can be obtained through a single matrix-vector product. The stabilizing approach based on a continuously variable α parameter is preferable when the HFF scheme with $\alpha = 1$ would make the system unstable, while the first technique can be advantageous when the system is stable but steady responses at the end of command steps are not verified at few actuation points. A further improvement of this term is related to its implementation, because Eq. (16) and, more in general, Eq. (18) do not assure the continuity of the static feed-forward contribution over different command steps. As a matter of fact, there is no guarantee that the average control force $\overline{\boldsymbol{f}}^c_{(k)}$ is equal to the FF static contribution computed at the same command step, i.e. $\boldsymbol{f}^c_{f_s(k)}$. This fact might degrade the system tracking capabilities, especially during the first transient phase, and, as a direct consequence, prevent the obtainment of a satisfactory steady state at the end of the command step. However, a better implementation of the HFF term allows to enforce the FF action continuity by rewriting Eq. 16 as

$$\boldsymbol{f}^c_{f_s(j)} = \boldsymbol{f}^c_{f_s(k)} + \left(\overline{\boldsymbol{f}}^c_{(k)} - \boldsymbol{f}^c_{f_s(k)} + \boldsymbol{K}^* \left(\boldsymbol{d}^r_{(k+1)} - \overline{\boldsymbol{p}}_{(k)}\right)\right) f_{sh}\left(t_{(j)}\right). \tag{22}$$

For the same reason it is better to modify Eq. (18) into

$$\boldsymbol{f}^c_{f_s((j)} = \boldsymbol{f}^c_{f_s(k)} + \Big([\diagdown \boldsymbol{\alpha} \diagup] \, \overline{\boldsymbol{f}}^c_{(k)} + (\boldsymbol{I} - [\diagdown \boldsymbol{\alpha} \diagup]) \, \boldsymbol{f}^c_{f_s(k)} - \boldsymbol{f}^c_{f_s(k)} \\ + \boldsymbol{K}^* \left(\boldsymbol{d}^r_{(k+1)} - \left([\diagdown \boldsymbol{\alpha} \diagup] \, \overline{\boldsymbol{p}}_{(k)} + (\boldsymbol{I} - [\diagdown \boldsymbol{\alpha} \diagup]) \, \boldsymbol{d}^r_{(k)} \right) \right) \Big) \, f_{sh}(t_{(j)}). \quad (23)$$

E. Identification of the feedforward matrices

The control strategy just described depends heavily on the FF contributions due to $\boldsymbol{K}^*$, $\boldsymbol{C}^*$ and $\boldsymbol{M}^*$. These matrices could be determined through appropriate numerical analyses, whereas a direct in the field identification will do far better in guaranteeing more robust and precise results.

In particular, the accuracy of $\boldsymbol{K}^*$ can significantly affect the achievement of precise positioning performances, even if the robustness of the HFF strategy can well cure an imprecise $\boldsymbol{K}^*$. As shown in [2], [15], matrix $\boldsymbol{K}^*$ can be accurately identified by resorting to very precise measures of the actuator forces and positions for at least $n_a + 1$ different commands. These measures can be obtained, without any feedforward, by computing adequately long averages over nominally steady conditions. The viability of such a precise identification has been verified numerically for mirrors with thousands of controlled points [2] and proven effective for already working DMs having several hundreds actuated points, such as the MMT and LBT. The remaining FF matrices $\boldsymbol{C}^*$ and $\boldsymbol{M}^*$ are better recovered through a divide et impera scheme applied to the equilibrium equations

$$\begin{bmatrix} \ddot{\boldsymbol{p}}^{f\,T} & \dot{\boldsymbol{p}}^{f\,T} \end{bmatrix} \begin{bmatrix} \boldsymbol{M}^{*T} \\ \boldsymbol{C}^{*T} \end{bmatrix} = \boldsymbol{f}^{c f\,T} - \boldsymbol{p}^{f T} \boldsymbol{K}^{*T}, \quad (24)$$

where $\boldsymbol{p}^f = filt(\boldsymbol{p})$ and $\boldsymbol{f}^{c\,f} = filt(\boldsymbol{f}^c)$ are the time histories of the positions and control forces filtered without introducing any phase error, either with an acausal symmetric FIR filter or through a forward-backward IIR filtering; the velocities, $\dot{\boldsymbol{p}}^f$, and accelerations, $\ddot{\boldsymbol{p}}^f$ are computed from the filtered position time histories, as explained below. The position filter should significantly remove any signal noise, so smoothing time histories, while limiting, as much as possible, any kind of phase distortion and amplitude attenuation within the frequency bandwidth described by the nominal model. In the present work a 4 kHz fourth order low-pass Butterworth filter has been used. Relying on the already identified $\boldsymbol{K}^*$ allows a substantial reduction of the parameters to be identified. Moreover, instead of adopting the standard approach [24], [25] that leads to $\boldsymbol{C}^*$ and $\boldsymbol{M}^*$ on the base of a single, adequately long

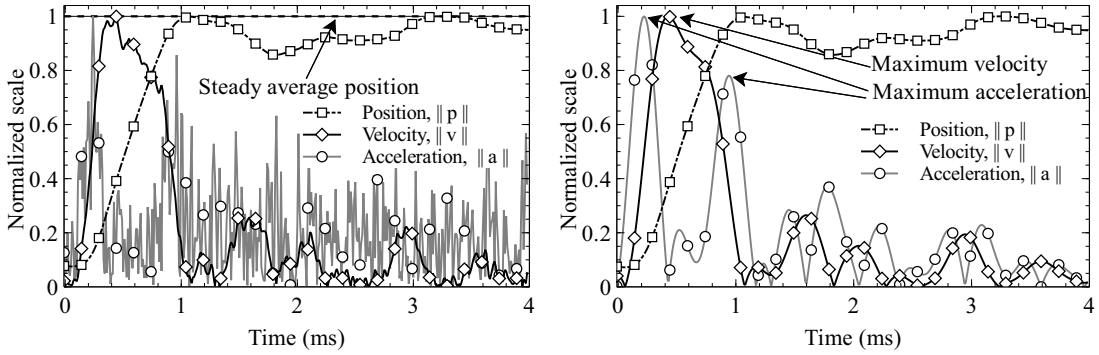

Figure 6. Typical behavior on a command step of position, velocity and acceleration absolute value (normalized to 1): unfiltered (left) vs. filtered (right) data.

and specific training history, they will be obtained by using the already available transient histories associated to the determination of $\boldsymbol{K}^*$. Such an approach leads to a really efficient and effective procedure, hopefully viable even for mirrors with thousands of controlled points. So, instead of writing Eq. (24) in excess of $2 \times n_a$ time instants of a single history, we write it for an equivalent number of times associated to a few of the most significant samples of all the positioning transients acquired while identifying $\boldsymbol{K}^*$. The velocities, $\dot{\boldsymbol{p}}^f$, and accelerations, $\ddot{\boldsymbol{p}}^f$, of each command response can be computed through a centered finite difference scheme applied to the filtered position vector $\boldsymbol{p}^f$. A typical result of such an operation is depicted in Figs. 6. It can be seen that, for each command transient, there is an initial high amplitude maximum for the velocity, v_{max}, and two maxima for the acceleration, $a_{max\,1}$ and $a_{max\,2}$, for each actuator. One can thus compute the average time instant at which the actuators reach maximum velocities, t_v, and the two corresponding time instants for the maximum accelerations, t_{a1} and t_{a2}.

By calling $\dot{\boldsymbol{p}}_1^{f_v}$, $\ddot{\boldsymbol{p}}_1^{f_{a1}}$ and $\ddot{\boldsymbol{p}}_1^{f_{a2}}$ the filtered velocities and accelerations computed at those time instants, Eq. (24) can be written for those three points of each command step, so that the related overdetermined system of equations becomes

$$\begin{bmatrix} \ddot{\boldsymbol{p}}_1^{f_v^T} & \dot{\boldsymbol{p}}_1^{f_v^T} \\ \ddot{\boldsymbol{p}}_1^{f_{a1}^T} & \dot{\boldsymbol{p}}_1^{f_{a1}^T} \\ \vdots & \vdots \\ \ddot{\boldsymbol{p}}_n^{f_{a2}^T} & \dot{\boldsymbol{p}}_n^{f_{a2}^T} \end{bmatrix} \begin{bmatrix} \boldsymbol{M}^{*^T} \\ \boldsymbol{C}^{*^T} \end{bmatrix} = \begin{bmatrix} \boldsymbol{f}_1^{cf_v^T} - \boldsymbol{p}_1^{f_v^T} \boldsymbol{K}^{*^T} \\ \boldsymbol{f}_1^{cf_{a1}^T} - \boldsymbol{p}_1^{f_{a1}^T} \boldsymbol{K}^{*^T} \\ \vdots \\ \boldsymbol{f}_n^{cf_{a2}^T} - \boldsymbol{p}_n^{f_{a2}^T} \boldsymbol{K}^{*^T} \end{bmatrix}, \tag{25}$$

where n is the number of command steps previously carried out for the identification of $\boldsymbol{K}^*$. The overdetermined system of Eq. (25) can be solved for $\boldsymbol{M}^*$ and $\boldsymbol{C}^*$ by using the very same recursive technique adopted to compute $\boldsymbol{K}^*$ [2].

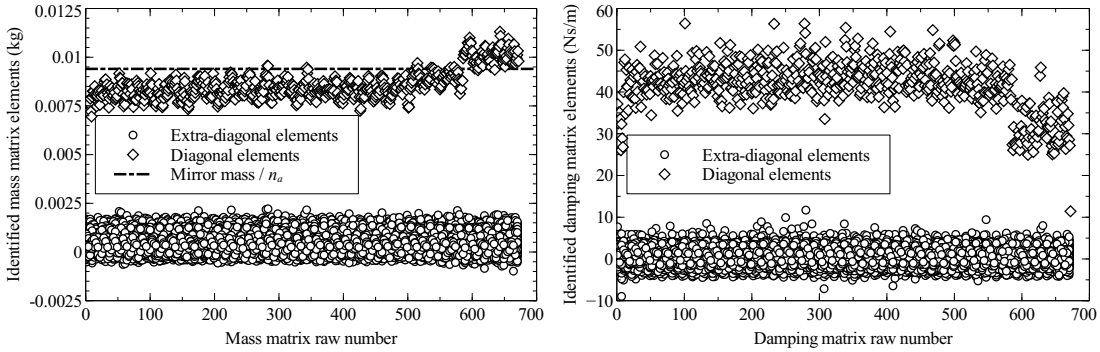

Figure 7. Elements of the GMT mirror identified mass (left) and damping (right) matrices.

The elements of the identified GMT mass and damping matrices are shown in Fig. 7. It should be noticed that both these matrices are diagonally dominant, thus confirming the dynamics uncoupling conjectured in [2]. Therefore the dynamic FF matrices can be assumed diagonal without significantly compromising the controller effectiveness. As hinted in [2], a rough estimate of the mass matrix could be built by associating to each actuation point a concentrated mass equal to 0.0094 kg, i.e. the total mirror mass divided by the number of actuation points. This leads to a diagonal mass characterized by a scalar parameter; Fig. 7 confirms the validity of this approximation. Even if such a choice is not taken the associated assumption provides a viable first check for verifying the goodness of the identified mass matrix.

F. Control system parameters optimization

The control scheme is composed by FF and feedback contributions. The PDD2 decentralized feedback requires the tuning of at least three parameters: G_a, G_v, G_p. The FF is already ideally self-tuned because the matrices have been identified in the field, but through a simplified model which is based on a quasi-steady fluid dynamic approximation and neglects system time delays and sensors/actuators dynamics; for this reason the dynamic FF action can be improved through the introduction of two scaling factors, λ_m and λ_c, applied to $\boldsymbol{M}^*$ and $\boldsymbol{C}^*$ respectively. An additional tunable parameter is the scaling factor α used to stabilize/optimize the HFF integral action, see Eq. 23. So a system with hundredths or thousandths of control points is finally reduced to the optimization of only six scalar parameters.

There is a wide choice of methods addressing the problem of tuning PD and PID controllers of SISO systems [26]; some of these techniques have been extended to MIMO systems as well, e.g. [27] [28]. A specific auto-tuning procedure for the system under evaluation is

proposed in [29], where just the PD gains are tuned through the optimization of identified modal transfer functions. A completely different approach is proposed here. The aim is to tune the feedback and FF parameters through a model free optimization to be carried out on the real system. Instead of looking for a globally optimal solution by a simultaneous optimization of all the control parameters [17], the strategy proposed here improves on an already suggested self-tuning [13], [15] by using a two steps optimization performed by repeatedly imposing a predefined training command vector time history $\boldsymbol{d}^r(t)$.

The first step tries to optimize the tracking performances by modifying the feedback gains and the dynamic FF parameters, $\boldsymbol{P} = \{G_a, G_v, G_p, \lambda_m, \lambda_c\}$. This optimization step should be performed with the telescope dome closed, i.e. avoiding as much as possible the presence of turbulence disturbances. In fact, in order to keep the system stable, it is not possible to set sufficiently high PDD2 gains to compensate for such disturbances. As shown in Sec. IV, turbulence disturbance is mainly rejected by the HFF integral action, which is the subject of the second optimization step, but should be switched off during this first step. The first step objective function to be minimized is the integral square error, computed only over the steady part of each training history command step, i.e.

$$J_{1_{opt}} = \min_{\boldsymbol{P}} \sum_{k=1}^{n_{step}} \sum_{j=j_{t_i}}^{j_{t_f}} \boldsymbol{e}_{(j)}^T(\boldsymbol{P}) \boldsymbol{e}_{(j)}(\boldsymbol{P}), \tag{26}$$

where n_{step} is the command steps number of the training command history, $\boldsymbol{e}_{(j)}$ is the $(n_a \times 1)$ vector of the tracking error of all actuators computed at the j^{th} control step inside the k^{th} step command, j_{t_i} is the control step where the steady part of each step command begins, while j_{t_f} is the last control step of each step command. If the interest is focused on tracking performances the reference command steps amplitude should be about one order of magnitude higher than the measurement noise, otherwise the optimization result moves toward a noise attenuating optimal solution. Considering the technology at hand, a step amplitude higher than 50 nm can be suggested. The command step length and the command shaping filter should be set equal to the operational one. An appropriately scaled realistic reference history can be considered a good choice. The objective function takes into account the tracking error retrieved only over the steady part of each command step in order to favor the achievement of a smoother tracking without overshoots [30], [26].

Evolutionary algorithms are ideal candidates for this kind of optimization because they are robust global search methods and can treat problems characterized by discontinuities, noises, and nonlinearities [31]. A genetic algorithm (GA) has been chosen, mainly because GAs have

already demonstrated to well fit the needs of control system tuning, see [32] and references therein. Typical GAs require the definition of bounds for all the optimization parameters and, within the user-defined bounds there can unavoidably be some parameters combination that leads to an unstable system. As stressed in [29], this is not a problem for the safety of the system, because the adaptive mirror is equipped with automatic safeguards that can deactivate the controller so to avoid any possible damage.

The optimization procedure has to converge toward a stable robust solution. The proposed technique exhibits a natural robustness because the objective function is evaluated directly on the real system, i.e. it is model free. Moreover the objective function computed only over the steady part of each command step is very sensitive to system oscillations and overshoots, that are usually induced by sets of parameters close to stability boundary. An insufficiently robust stable solution can be achieved whenever the identified static FF matrix $\boldsymbol{K}^*$ is affected by significant errors. This is because the optimizer can only try to augment the proportional gain in order to compensate for steady position errors, thus moving the system toward instability. This undesirable situation is usually avoided thanks to the fact that the identification procedure of the static FF matrix does lead to accurate results. Anyway, if necessary, it is possible to run a pre-training phase during which the very accurate static FF forces required to reach commanded positions are determined and stored. This task can be easily accomplished by repeatedly imposing the same command step and by exploiting the capability of the HFF to cancel position errors, so that the exact required static forces can be found.

Once the first optimized parameters set $\boldsymbol{P}_{opt}$ has been obtained through a GA, it is possible to refine it by performing a local optimization. We explored the use of the Nelder-Mead simplex algorithm [33], [34], [35] and of the Bound Optimization by Quadratic Approximation code (BOBYQA) [36]. The first one is a direct search method that does not require information about problem gradients and guarantees robustness with respect to discontinuous and noisy problem domains; for this reason it is well suited for the problem at hand, which is based on experimental measurements. The second one is a derivative-free optimization solver for nonlinear problems characterized by a large parameters set. This method proved to be more efficient than Nelder-Mead, but less robust when the objective function is noisy; this often led BOBYQA to higher values of $\boldsymbol{P}_{opt}$, but without appreciable loss of performances.

The same parameters can be adopted for all the DM control points; this simplifies the system tuning and speeds up the optimization procedure. Alternatively, better system performances can be obtained with variable parameters along the radial direction. This allows

to account for a somewhat reduced fluid dynamic damping close to internal and external mirror borders, where the air cushion is freely connected to atmosphere. For this reason it is advisable to associate the actuation points of different radial regions to different parameter sets.

The second optimization step aims at improving disturbances rejection and to assure the stability of the HFF contribution by searching an optimal value of α, see Eq. 23. The procedure is similar to the first step, but now the objective function is computed over all the command steps length, i.e. $j_{t_i} = 1$, and the parameter that has to be tuned is scalar. In this second phase the turbulence disturbance can be approximated following the simplified model described in [4], with the simulated disturbance forces reproduced at each actuation points. This second optimization step may require even longer training histories in order to guarantee a correct stochastic description of turbulence disturbances. Nevertheless, this single parameter optimization is quite easy to be solved, so it is possible to profitably use all the previously mentioned optimization methods. GAs and BOBYQA manage bound-constrained problems, so they can guarantee a final solution, α_{opt}, within the range $[0 - 1]$.

Simulations of the self-tuning procedure are reported in Sec. IV. An approximated state-space fluid dynamic model has been used to reduce the computational cost.

G. System stability

Possible instabilities due to the HFF have been discussed in Section III-D, along with two possible stabilizing solutions. The ideally co-located feedback contribution can not induce any kind of instability if true displacements, velocities and accelerations are available at the control points. Unfortunately, co-location is far from ideal and the passband action of sensors/actuators and pseudo-derivatives, combined with digital controller delays, introduce destabilizing elements. For this reason it is mandatory to assess the overall stability of the controlled system, as well as the effectiveness of the feedback gains set in assuring appropriate performances. A straightforward way to proceed is represented by the use of a numerical simulator, based on the very accurate system modeling described at the beginning of the paper (see [4], [2], [3] for more details). The simulator ability to reproduce realistic results has been verified through numerical/experimental correlations [14], [15]. Nevertheless, any numerical model represents a simplified description of the reality; for this reason, starting from safe values suggested by numerical analyses, a final feedback gains tuning must always be performed in the field, as suggested in Sec.III-F.

Parameters	Curve 2	Curve 3	Curve 4
$\lceil \boldsymbol{G}_p \rfloor$ (N/m)	$\lceil 20000 \rfloor$	$\lceil 20000 \rfloor$	$\lceil 20000 \rfloor$
$\lceil \boldsymbol{G}_v \rfloor$ (N·s/m)	$\lceil 8 \rfloor$	$\lceil 8 \rfloor$	$\lceil 8 \rfloor$
$\lceil \boldsymbol{G}_a \rfloor$ (kg)	$\lceil 2\text{E}-4 \rfloor$	$\lceil 2\text{E}-4 \rfloor$	$\lceil 2\text{E}-4 \rfloor$
n_m^h	4300	4300	4300
ω_h^{min} (rad/s)	4263·2π	4263·2π	4263·2π
ω_h^{max} (rad/s)	32400·2π	32400·2π	32400·2π
$\xi_h(\omega_h^{min})$	0.01	0.01	0.01
$\xi_h(\omega_h^{max})$	0.0001	0.0001	0.0001
ω_a (rad/s)	15000·2π	3000·2π	3000·2π
ω_s (rad/s)	15000·2π	3000·2π	3000·2π
ω_v (rad/s)	15000·2π	4000·2π	4000·2π
Spatial filter	no	no	yes

Table I

CONTROLLED SYSTEM PARAMETERS USED TO BUILD THE CURVES OF FIG. 9.

Despite these considerations, whenever the simulator is exploited to study the behavior of new DMs, it is important to verify that it is possible to reach adequate performances with a gains set assuring stability robustness to model uncertainties. Moreover, such robustness analysis can be of help to better quantify how all of the time and spatial filters affect stability. The description of the system dynamics usually involves high-frequency uncertainties and truncation. For the case at hand the main uncertainties are related to the high-frequency structural and squeeze film behavior. A possible way to handle the problem is shown in Fig. 8(a), where the nominal plant description $\boldsymbol{G}_n$ is introduced along with the high-frequency uncertainties $\boldsymbol{G}_h$. $\boldsymbol{F}_a$ and $\boldsymbol{F}_s$ are the same $(n_a \times n_a)$ diagonal transfer matrices describing the actuator and sensor dynamics in Fig. 5. Here they are interpreted as design degrees of freedom, which allow to appropriately filter the control forces and sensor measurements in order to achieve a satisfactory stability robustness. These filters are modeled as uncoupled first order low-pass dynamic systems characterized respectively by cutoff circular frequencies ω_a and ω_s. $\boldsymbol{C}_{tc}$ is a continuous time approximation of the $(n_a \times n_a)$ PDD2 controller transfer function of Eq. 5 and of the HFF integral contribution

$$\boldsymbol{C}_{ct} = \lceil \boldsymbol{G}_p \rfloor + \lceil \boldsymbol{G}_v \rfloor \frac{s\omega_v}{s+\omega_v} + \lceil \boldsymbol{G}_a \rfloor \frac{s^2\omega_v^2}{(s+\omega_v)^2} + \boldsymbol{G}_i \frac{1}{s}, \tag{27}$$

where ω_v is the pseudo-derivative cutoff frequency, here approximated through a first order dynamic filter for both the first and second derivative, $\boldsymbol{G}_i = \frac{\alpha}{dt_c}(\boldsymbol{K}^* + \lceil \boldsymbol{G}_p \rfloor)$ is a rough

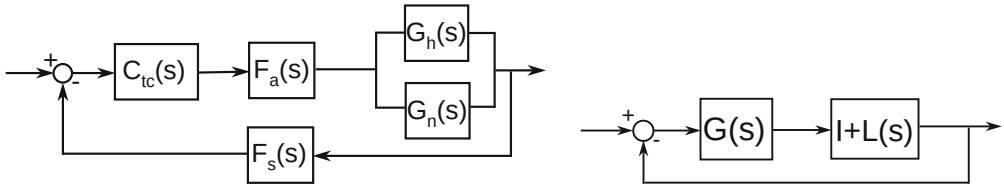

(a) Simplified model description with additive uncertainty. (b) Multiplicative uncertainty representation.

Figure 8. The simplified block diagrams used for assessing the control system stability robustness.

continuous time approximation of the HFF integral contribution, with $dt_c = 5\text{E}-4$ s the system command rate and $\alpha = 0.75$. $\boldsymbol{G}_n$ is the $(n_a \times n_a)$ approximated quasi-steady system transfer matrix already introduced in Sec. III-C; $\boldsymbol{G}_h$ is the $(n_a \times n_a)$ transfer matrix modeling the residual high-frequency dynamics

$$\boldsymbol{G}_h = \boldsymbol{X}_h \left[\diagdown \frac{1}{s^2 + 2\xi_h \omega_h s + \omega_h^2} \diagdown \right] \boldsymbol{X}_h^T, \tag{28}$$

where $\boldsymbol{X}_h$ is the $(n_a \times n_m^h)$ high-frequency modal matrix containing the n_m^h modal shapes that are not correctly described by $\boldsymbol{G}_n$; ω_h and ξ_h are the natural frequencies and damping coefficients of each neglected modal shape. We assume that the nominal model description is the more accurate the lower the frequency. Matrix $\boldsymbol{G}_h$ is thus linearly interpolated, for frequencies ranging from 3500 to 0 Hz, between that of Eq. 28 and a very low value. The fluid dynamics action is approximated by conservatively tuning the damping coefficient values ξ_h, assumed as linearly varying between the lowest and highest residual modal frequency, ω_h^{min} and ω_h^{max}. The high-frequency modal parameters are reported in Tab. I.

In [37] it is shown how the block diagram of Fig. 8(a) can be represented, as for Fig. 8(b), through a multiplicative uncertainty exploiting the $(n_a \times n_a)$ transfer matrices $\boldsymbol{G} = \overline{\boldsymbol{G}}_n \boldsymbol{C}_{tc}$ and $\boldsymbol{L} = \overline{\boldsymbol{G}}_h \overline{\boldsymbol{G}}_n^{-1}$, with $\overline{\boldsymbol{G}}_h = \boldsymbol{F}_s \boldsymbol{G}_h \boldsymbol{F}_a$ and $\overline{\boldsymbol{G}}_n = \boldsymbol{F}_s \boldsymbol{G}_n \boldsymbol{F}_a$. Once the nominal system stability has been verified, i.e. the design based on $\boldsymbol{G}_n$, the MIMO robust theory guarantees the stability of the plant perturbed through the introduction of the uncertainties when [38]

$$\overline{\sigma}\left(\boldsymbol{G}(j\omega)\left(\boldsymbol{I} + \boldsymbol{G}(j\omega)\right)^{-1}\right) < 1/\overline{\sigma}\left(\boldsymbol{L}(j\omega)\right) \qquad \forall \omega > 0. \tag{29}$$

Eq. 29 measures the system stability robustness for uncertainties at the plant output. The nominal plant stability can be easily verified by computing the eigenvalues of its state space realization. The allowable gains assuring stability are very high because of the high fluid dynamic damping granted within the frequency band represented by the nominal plant, i.e. about $(0 - 4200)$ Hz. In fact, the nominal model damping ratios show an average monotonic decay within the range $[0.7 - 0.05]$; so setting $\xi_h(\omega_h^{min}) = 0.01$ represents a conservative

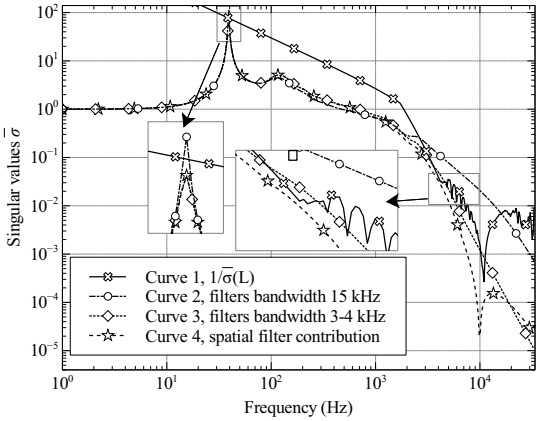

Figure 9. Stability evaluation of the perturbed controlled system.

choice to take into account the well known uncertainty which always involves high frequency damping estimation. On the contrary the stability verification in presence of high-frequency dynamics imposes severe limitations to the controller gains. The stability is highly affected by the measurements and control forces filters, as well as by the pseudo-derivative cutoff frequency. Fig. 9 allows to graphically verify Eq. 29, with curve 1 representing $1/\overline{\sigma}(L)$ and curves 2, 3 and 4 the trend obtained for $\overline{\sigma}\left(\boldsymbol{G}\left(\boldsymbol{I}+\boldsymbol{G}\right)^{-1}\right)$, with a nominal system characterized by the same PDD2 gains but different filters bandwidth (see Tab. I). Curve 2 is obtained with filters cutoff frequencies of 15 kHz. It is clear that the perturbed system does not verify the robust stability criterion. Looking at curve 3, one notices that important improvements can be obtained by lowering the measurements and control forces filtering bandwidth to 3 kHz and setting the pseudo-derivative cutoff frequency at 4 kHz. Nevertheless, this is apparently not sufficient to satisfy the robust stability condition and a further reduction of the filters bandwidth would badly affect the system performances.

Curves 2 and 3 have been obtained by assuming ideally co-located sensors measurements. However, numerical simulations accounting for the distributed sensor measurement confirm a non negligible influence on system stability. This is because the distributed nature of sensors introduces a band stop spatial filter, which helps attenuating the modal resonances within a critical frequency band. An easy way, albeit approximated, to understand the action of the spatial filter is to linearize each i^{th} component of the measured mirror displacements, $p_{(i)}$, with respect to the capacitors plates distances x_{nc} around the flat mirror configuration, so obtaining

$$p_{(i)} \approx p_{0(i)} + \frac{\int_{\Sigma(i)} \mathrm{d}x_{nc}\, d\Sigma}{A_{(i)}} = p_{0(i)} + \mathrm{d}p_{(i)}, \tag{30}$$

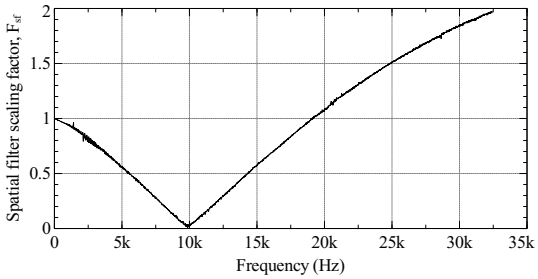

Figure 10. Spatial filter scaling factor, averaged over all the actuation points.

where $A_{(i)}$ is the i^{th} capacitor plate area and d$p_{(i)}$ is the variation of the i^{th} non co-located sensor measurement. Eq. 30 simply shows that the linearly approximated variation of the measured positions is equal to the averaged variation of the capacitors plates distances. For such a reason the measured displacements induced by a modal shape can be approximated as the averaged modal shape deformation over the capacitors plate areas. An average approximated measure of the filtering action due to the distributed nature of the capacitors plates can be computed as

$$F_{sf_j} = \frac{1}{n_{act}} \sum_{i=1}^{n_{act}} \|\tilde{\boldsymbol{X}}_{ij}\| / \|\boldsymbol{X}_{ij}\|, \tag{31}$$

where the index i refers to the i^{th} actuation point, j to the j^{th} modal shape and $\tilde{\boldsymbol{X}}_{ij}$ is the non co-located linearized measured displacement of the i^{th} actuator associated to the j^{th} modal shape. F_{sf_j} is a spatial filter scaling factor averaged over all the actuation points for the j^{th} modal deformation. Fig. 10 reports the scaling factor F_{sfj} defined above as a function of the corresponding modal frequency. It is evident that the sensors finite size have a band stop action over a relatively wide frequency range. The maximum attenuation is very close to the peak of the residual dynamics uncertainties, thus improving the system stability robustness. However, there is an amplification effect ($F_{sf} > 1$) at higher frequencies, and this could endanger the overall stability of the system. Nonetheless introducing the filter action as a not delayed scaling factor of the sensor measurements in the computation of the system transfer matrices $\overline{\boldsymbol{G}}_a$ and $\overline{\boldsymbol{G}}_h$, one obtains the curve 4 of Fig. 9, which satisfies the robust stability test. This confirms that the sensors spatial filtering action is important in enhancing stability margin and that it could even be considered an added design parameter, allowing to better tune the controlled system behavior and performances [39][40]. It is here remarked that a rigorous analysis of the spatial filter effect would require the computation of the full system transfer matrix, which is computationally too demanding for the case at hand. However, on

the basis of the here presented approach, an approximated frequency weight can be estimated and exploited for the stability robustness analysis. The weight is applied as a scalar scaling factor, so supposing the absence of phase lags, which is for sure a further approximation, especially at high frequencies; but the presence of three first order low-pass filters with very low corner frequencies (3 - 4 kHz) should encompass most of the phase delay within the most critical frequency bandwidth where the robust stability is verified.

The gains used for Fig. 9 can be regarded as a limit choice, because its depicted stability robustness with respect to uncertainties is represented by the lowest distance between the curves 1 and 4, which is quite tight. Nonetheless it should be taken into account that the proposed unstructured description of uncertainties is a severely conservative choice. This is in accordance with the fact that higher gains can be safely used in numerical simulations and, more significantly, on real already operative systems of comparable dimensions, such as the MMT and LBT secondary DMs. In order to warrant a well working system it is nonetheless important to verify, through high fidelity simulations that the system can assure satisfactory performances even with such a robust gains set.

The nominal plant and the feedback continuous time approximation can also be exploited to check the control system bandwidth in presence of gains assuring robust stability. Some useful considerations can be added with respect to the role of the integral contribution, i.e. the advantages of the HFF centralized structure with respect to a completely decentralized PIDD2 implementation. The control bandwidth can be estimated through the singular values computation of the system sensitivity matrix transfer function $\boldsymbol{S}(\boldsymbol{s}) = (\boldsymbol{I} + \boldsymbol{G})^{-1}$. The maximum and minimum singular value are associated to the worst and best directions [41], respectively. They are shown in Fig 11 for a completely decentralized PDD2, a completely decentralized PIDD2 and the proposed HFF integral contribution approximation plus decentralized PDD2 control. The adopted gains are those of Tab. I, with the decentralized integral gain of 3.E7 N/(ms) and the HFF stabilizing parameter $\alpha = 0.75$ chosen in such a way to satisfy both the nominal plant stability and the stability robustness criteria. It is clear that the PDD2 does not guarantee the system tracking for some directions that are always above the limit of $1/\sqrt{2}$. The PIDD2 bandwidth varies between 1 Hz and 153 Hz, the HFF one between 19 Hz and 305 Hz. The HFF solution improves the worst case direction bandwidth by more than an order of magnitude, and doubles the best case bandwidth. In any case the feedback bandwidth is well below 2 kHz and the tracking of a 2 kHz command history is possible only thanks to the feedforward contributions. Figure 11 also highlights that the introduction

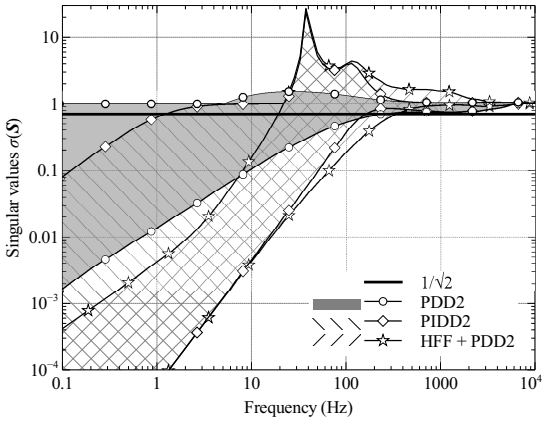

Figure 11. Approximated time-continuous GMT control system bandwidth with robust gains set.

of an integral term brings a sensitivity peak that, despite Eq. (29) being verified, suggests a somewhat reduced stability robustness.

IV. Simulation results

The presented results refer to the GMT on-axis secondary adaptive mirror. This mirror has 672 actuation points (see Fig. 3); all the details of the model can be found in [4]. In order to model realistic manufacturing tolerances of the reference plane, the initial gap between the shell and the reference plane has been set with a profile variable within (50-100) μm. Figs. 12 report the system performances that are achievable with the robustly stable gains set found in Sec. III-G, and with the filters bandwidth, as well as the pseudo-derivative realization, suggested in Tab. I, Curve 4. The sensor non-co-located measurement time history of an actuation point plotted in Fig. 12 highlights the tracking capability of a 2 kHz step reference command; the command history is in accordance with a median seeing condition and has been provided by the GMT working group. The enhanced tracking, achieved by exploiting the identified dynamic FF matrices with respect to constant diagonal ones, is evident. Such a result is mainly due to a better compensation of the system own dynamics thanks to the identified matrix $\boldsymbol{C}^*$, which can better fit the system damping associated to the variable fluid film thickness and the boundary conditions. The rms tracking error of Fig. 12 is computed over all the actuation points and confirms a global improvement of the system performances: an rms positioning error below 10 nm at the end of each command step is found.

The previous results have been obtained without external disturbances. The results obtained in presence of turbulence with different HFF stabilization techniques are reported in

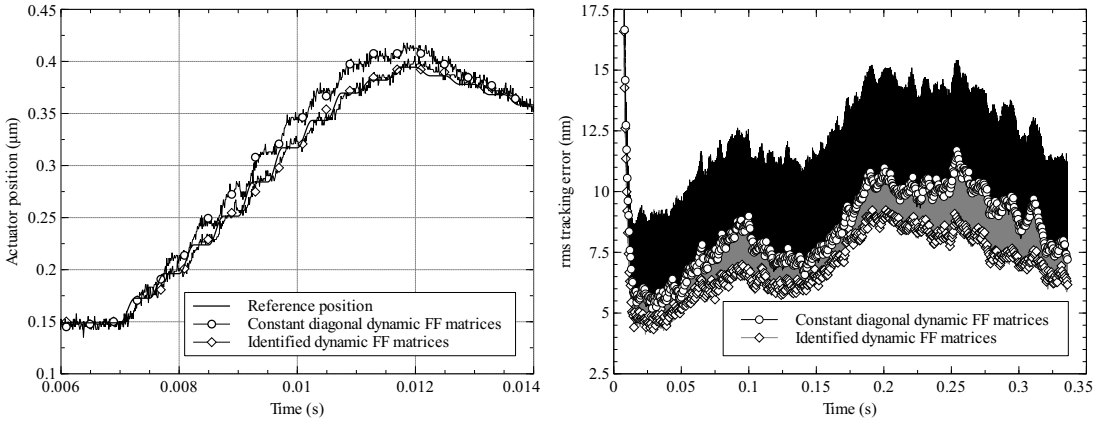

Figure 12. Comparison of the system tracking performances using constant diagonal and identified dynamic FF matrices.

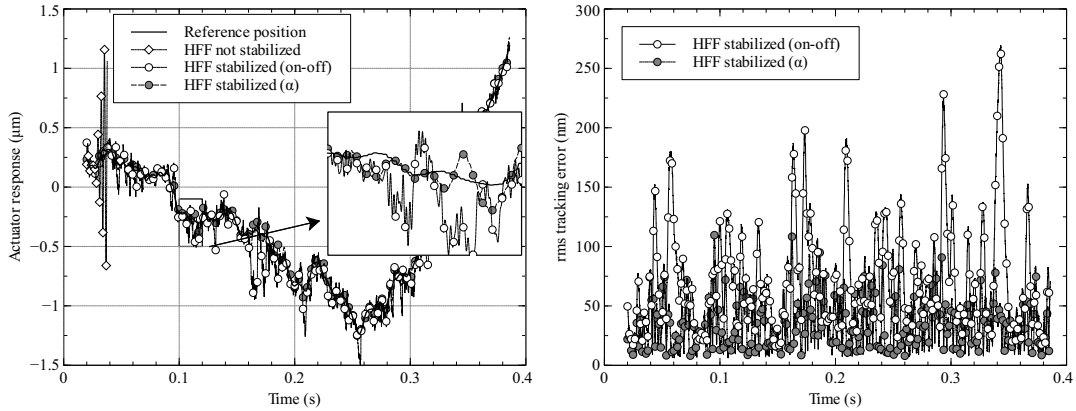

Figure 13. Comparison of system performances in presence of turbulence with different HFF stabilization techniques (on-off = HFF deactivation based on standard deviation boundary; α = HFF stabilization through integral gain scaling parameter α)

Figs. 13. Based on the experimental measurements performed on the Gemini telescope [42], we suppose a turbulence average velocity of 7.5 m/s and a velocity standard deviation of 2 m/s, see [4] for details. The time history of Fig. 13 highlights that the system is unstable when no stabilization is provided for the HFF contribution. With the stabilization turned on, the approach that simply switch on and off the HFF (on-off scheme in Figs. 13) leads to an higher rms error, because of the introduction of an implicit discontinuous control law. On the contrary a constant $\alpha = 0.75$ parameter (α scheme in Figs. 13) can assure stability as well as a smoother signal tracking. In this way average and absolute rms tracking error can be kept lower, as shown in Fig. 13.

Figs. 14 highlight the optimization capabilities of the proposed procedure. The five feed-

back and FF parameters, considered constant for all the actuation units (single sector optimization), have been retrieved through a GA optimization based on a population of 50 individuals. The solution converged after 141 generations. The objective functions have been computed on the basis of a five steps training history at a 2 kHz command rate. It is of utmost importance to remark that the same optimization on the real system will require less than 20 s, so that an even better in the field tuning is possible, e.g. longer command histories. The optimal solution has been further refined through a Nelder-Mead scheme, which required about 400 further objective functions evaluation. Eventually, the mirror actuation points have been subdivided into three different circular sectors characterized by different parameters values and a second optimization has been performed (3 sectors optimization). The parameters range for the GA was centered ($\pm 20\%$) around the single sector optimization result. The optimal gains have been tested on the same command history used for previous analysis. The results are reported in Fig. 14. Note that the optimization, as well as the time histories of Fig. 14 are based on a simplified system simulator, without a realistic fluid dynamics description, as specified in Sec. III-F. For this reason the results are not directly comparable with the previous ones. The tracking performances obtained by using one or three circular sectors appear very similar, even if the rms tracking error presented in Fig. 14 shows that a small improvement is brought by the three sectors solution. Finally the optimization of the α parameter has been computed with both the GA and the BOBYQA codes. Here the objective function, computed in presence of turbulence, is based on 50 steps of a median seeing command history. Both the optimization techniques gave comparable results, with an optimal α value around 0.8. The optimal solution is very close to what has been found by manually adjusting the gains with a long and cumbersome trial and error manual procedure.

V. Concluding remarks

This paper is focused on the development of a control technique suitable to obtain sub-microshaping of secondary adaptive mirrors. The control strategy is an improvement of the procedure presented in [2]. The work strives to keep the feedforward-based implementation of the integral contribution without splitting it from the pure feedforward one. While the integral contribution can give rise to instabilities, they are kept under control by proposing two different stabilization techniques. The effects of filtering the measurements and control forces on the system stability robustness are highlighted, together with the fundamental band-stop spatial filter action introduced by the actual finite size of the capacitive position sensors.

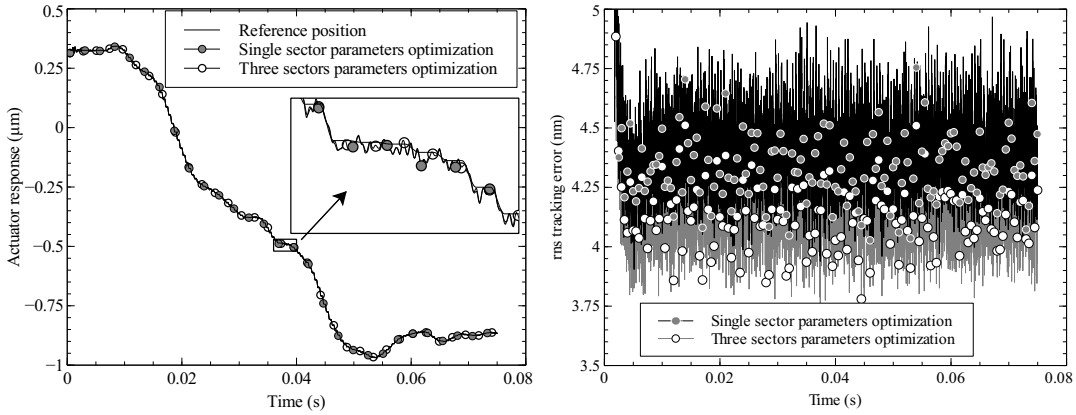

Figure 14. Comparison of system tracking performances using controller parameters optimized with a single sector, i.e. parameters equal for all actuation units, and three sectors.

The control system is self-tuning. As a first step, all the FF matrices can be identified in the field. Then, the feedback gains and few FF tuning parameters can be optimized automatically. The proposed control law performances are verified through high-fidelity simulations of the on-axis GMT secondary adaptive mirror. Despite the fact that the optimization reliability has been verified on a simplified system model to keep the simulation time reasonably low, the simulations confirm that the optimization procedure does work and actually allows to obtain a completely self-tuned controller. It has been verified that the system has acceptable performances even if decentralized feedback gains assuring stability robustness are used instead of the optimized ones. While the real system is supposed to work with an optimized gain set, and not with the robust one, this gives confidence on the overall feasibility of the project with respect to modeling errors of the system simulator. These results should be of help in expediting the application of the non-contacting adaptive technology to future extremely large telescopes, and possibly for the control of different typologies of massively controlled flexible structures.

ACKNOWLEDGMENTS

The support of Microgate, ADS International and GMTO Corporation in providing information and data needed for the present paper is gratefully acknowledged.

REFERENCES

[1] J. Hardy, *Adaptive Optics for Astronomical Telescopes*. New York: Oxford University Press, 1998.

[2] M. Manetti, M. Morandini, and P. Mantegazza, "High precision massive shape control of magnetically levitated adaptive mirrors," *Control Engineering Practice*, vol. 18, no. 12, pp. 1386–1398, Dec. 2010.

[3] M. Manetti, "High precision shape control of masssively actuated, magnetically levitated, secondary adaptive mirrors for extremely large telescopes," Ph.D. Thesis, Politecnico di Milano, Milano, Feb 2011.

[4] M. Manetti, M. Morandini, and P. Mantegazza, "Servo-fluid-elastic modeling of contactless levitated adaptive secondary mirrors," *Computational Mechanics*, Dec. 2011.

[5] F. P. Wildi, G. Brusa, M. Lloyd-Hart, L. M. Close, and A. Riccardi, "First light of the 6.5-m MMT adaptive optics system," in *Astronomical Adaptive Optics Systems and Applications*, R. Tyson and M. Lloyd-Hart, Eds., vol. 5169. San Diego, CA, USA: SPIE, Dec. 2003, pp. 17–25.

[6] A. Riccardi, G. Brusa, P. Salinari, S. Busoni, O. Lardiere, P. Ranfagni *et al.*, "Adaptive secondary mirrors for the large binocular telescope," in *Proceedings SPIE, Astronomical Adaptive Optics Systems and Applications*, San Diego, USA, August 2003.

[7] G. Stein and D. Gorinevsky, "Design of surface shape control for large two-dimensional arrays," *Control Systems Technology, IEEE Transactions on*, vol. 13, no. 3, pp. 422–433, 2005.

[8] J. Kulkarni, R. D'Andrea, B. Brandl, P. Wizinowich, and D. Bonaccini, "Application of distributed control techniques to the adaptive secondary mirror of Cornell's Large Atacama Telescope," in *Adaptive Optical System Technologies II*, vol. 4839. Waikoloa, HI, USA: SPIE, Feb. 2003, pp. 750–756.

[9] P. Massioni and M. Verhaegen, "Distributed control for identical dynamically coupled systems: A decomposition approach," *Automatic Control, IEEE Transactions on*, vol. 54, no. 1, pp. 124–135, 2009.

[10] R. Ellenbroek, M. Verhaegen, N. Doelman, R. Hamelinck, N. Rosielle, M. Steinbuch, B. L. Ellerbroek, and D. B. Calia, "Distributed control in adaptive optics: Deformable mirror and turbulence modeling," in *Advances in Adaptive Optics II*, vol. 6272. Orlando, FL, USA: SPIE, Jun. 2006.

[11] R. Heimsten, M. Owner-Petersen, T. Ruppel, D. G. MacMynowski, and T. Andersen, "Suppressing low-order eigenmodes with local control for deformable mirrors," *Optical Engineering*, vol. 51, no. 2, p. 026601, 2012.

[12] A. H. Bouchez, D. S. Acton, G. Agapito, C. Arcidiacono, F. Bennet, V. Biliotti *et al.*, "The Giant Magellan Telescope adaptive optics program," in *Adaptive Optics Systems III*, vol. 8447. Amsterdam: SPIE, 2012.

[13] M. Manetti, M. Morandini, P. Mantegazza, R. Biasi, D. Gallieni, and A. Riccardi, "Modeling and control of massively actuated, magnetically levitated, adaptive mirrors," in *Control Applications (CCA), 2010 IEEE International Conference on*, 2010, pp. 860–866.

[14] M. Manetti, M. Morandini, P. Mantegazza, R. Biasi, D. Gallieni, and A. Riccardi, "Experimental validation of a numerical model for non-contact, massively actuated deformable adaptive mirrors," in *Proc. SPIE*, vol. 7736, San Diego, California, USA, 2010.

[15] M. Manetti, M. Morandini, P. Mantegazza, R. Biasi, D. Gallieni, and A. Riccardi, "Experimental validation of massively actuated deformable adaptive mirror numerical models," *Control Engineering Practice*, 2012.

[16] S. Skogestad and I. Postlethwaite, *Multivariable Feedback Control Analysis and Design*. John Wiley & Sons Ltd, 1996.

[17] A. Mituhiko and T. Hidefumi, "Two-Degree-of-Freedom PID controllers," *International Journal of Control, Automation, and Systems*, vol. 1, no. 4, pp. 401—411, 2003.

[18] C. An, C. Atkeson, J. Griffiths, and J. Hollerbach, "Experimental evaluation of feedforward and computed torque control," *IEEE Transactions on Robotics and Automation*, vol. 5, no. 3, pp. 368–373, 1989.

[19] V. Santibanez and R. Kelly, "PD control with feedforward compensation for robot manipulators: analysis and experimentation," *Robotica*, vol. 19, no. 1, pp. 11–19, 2001.

[20] F. Lewis, D. Dawson, and C. Abdallah, *Robot Manipulator Control: Theory and Practice*. CRC Press, 2004.

[21] M. Morari and E. Zafiriou, *Robust Process Control*. Prentice-Hall, 1989.

[22] G. Brusa-Zappellini, A. Riccardi, S. Ragland, S. Esposito, C. Del Vecchio, L. Fini *et al.*, "Adaptive secondary p30 prototype: Laboratory results," in *Proceedings SPIE, Adaptive Optical System Technologies*, Kona, Hawaii, September 1998, pp. 764–775.

[23] G. F. Franklin, J. D. Powell, and M. L. Workman, *Digital Control of Dynamic Systems*, 3rd ed. Addison-Wesley, Dec. 1997.

[24] K. Astrom and B. Wittenmark, *Adaptive Control*. Addison-Wesley, 1989.

[25] E. Nissim and G. Gilyard, "Method for experimental determination of flutter speed by parameter identification," NASA, Technical Paper 2923, 1989.

[26] K. Astrom and T. Hagglund, *PID Controllers: Theory, Design, and Tuning*, 2nd ed. ISA: The Instrumentation, Systems, and Automation Society, Jan. 1995.

[27] A. P. Loh, W. W. Tan, and V. U. Vasnani, "Relay feedback of multivariable systems and its use for auto-tuning of multi-loop PI controllers," in *International Conference on Control, 1994. Control '94*, vol. 2. IET, Mar. 1994, pp. 1049–1054.

[28] Y. Halevi, Z. J. Palmor, and T. Efrati, "Automatic tuning of decentralized PID controllers for MIMO processes," *Journal of Process Control*, vol. 7, no. 2, pp. 119–128, 1997.

[29] G. Agapito, S. Baldi, G. Battistelli, D. Mari, E. Mosca, and A. Riccardi, "Automatic tuning of the internal position control of an adaptive secondary mirror," *European Journal of Control*, vol. 17, no. 3, pp. 273–289, Jun. 2011.

[30] O. Lequin, M. Gevers, M. Mossberg, E. Bosmans, and L. Triest, "Iterative feedback tuning of PID parameters: Comparison with classical tuning rules," *Control Engineering Practice*, vol. 11, no. 9, pp. 1023–1033, Sep. 2003.

[31] M. W. Iruthayarajan and S. Baskar, "Evolutionary algorithms based design of multivariable PID controller," *Expert Systems with Applications*, vol. 36, no. 5, pp. 9159–9167, Jul. 2009.

[32] C. Vlachos, D. Williams, and J. B. Gomm, "Genetic approach to decentralised PI controller tuning for multivariable processes," *Control Theory and Applications, IEE Proceedings* -, vol. 146, no. 1, pp. 58–64, Jan. 1999.

[33] J. A. Nelder and R. Mead, "A simplex method for function minimization," *The Computer Journal*, vol. 7, no. 4, pp. 308–313, jan 1965.

[34] *Matlab Optimization Toolbox User's Guide R2012a*. MathWorks, Matlab, 2012.

[35] J. Nocedal and S. Wright, *Numerical Optimization*, ser. Springer Series in Operations Research and Financial Engineering. Springer, 2006.

[36] M. Powell, "The BOBYQA algorithm for bound constrained optimization without derivatives," Centre for Mathematical Sciences, University of Cambridge, UK, Tech. Rep. DAMTP 2009/NA06, 2009.

[37] R. Bastaits, G. Rodrigues, B. Mokrani, and A. Preumont, "Active optics of large segmented mirrors: Dynamics and control," *Journal of Guidance, Control, and Dynamics*, vol. 32, no. 6, pp. 1795–1803, Nov. 2009.

[38] J. Doyle and G. Stein, "Multivariable feedback design: Concepts for a classical/modern synthesis," *IEEE Transactions on Automatic Control*, vol. 26, no. 1, pp. 4– 16, Feb. 1981.

[39] S. Collins, D. Miller, and A. Von Flotow, "Distributed sensors as spatial filters in active structural control," *Journal of Sound and Vibration*, vol. 173, no. 4, pp. 471–501, Jun. 1994.

[40] J. Sullivan, J. Hubbard, and S. Burke, "Distributed sensor/actuator design for plates: Spatial shape and shading as design parameters," *Journal of Sound and Vibration*, 1997.

[41] S. Skogestad and I. Postlethwaite, *Multivariable feedback control: analysis and design*, 2nd ed. Wiley, Aug. 2001. [Online]. Available: http://alexandria.tue.nl/openaccess/Metis208895.pdf

[42] D. Smith, "Gemini south wind data," 2001, http://www.tuc.noao.edu/system/gsmt/studies/.